Machine Learning-Enhanced Fingertip Tactile Sensing: From Contact Estimation to Reconstruction

Zhongjin Xu

Department of Electrical and Computer Engineering, University of Michigan-Dearborn, MI 48128, USA;

zhongjin@umich.edu

*Corresponding Author: zhongjin@umich.edu

DOI: https://doi.org/10.30212/JITI.202503.007

Submitted: Mar. 23, 2024 Accepted: May. 6, 2025

ABSTRACT

Fingertip tactile sensing is a crucial perceptual mechanism for both humans and robots, providing valuable data on contact detection, force feedback, and object properties such as surface texture, shape, and temperature. This paper presents a novel tactile sensing system that incorporates a six-axis force/torque sensor, combined with innovative methods to harness force and torque signals for enhanced tactile perception. The main contributions of this work are as follows: (1) we propose a new approach for determining contact positions and normals, identifying unintended movements, and analyzing surface texture features, (2) we introduce a technique for estimating an object's center of gravity (CoG), which is integrated with tactile sensing for more accurate object interaction, and (3) we integrate a machine learning framework using an artificial neural network to classify objects based on CoG estimations and tactile data. Finally, we demonstrate the effectiveness of the proposed system through object reconstruction examples, confirming its performance in real-world applications.

Keywords: Tactile sensing, Six-axis force/Torque sensor, Contact detection, Center of gravity estimation, Machine learning integration, Object classification

1. Introduction

Tactile sensing is a cornerstone of robotic perception, with fingertip sensors playing an especially pivotal role in enhancing the dexterity and functionality of robotic hands. Over the past several decades, researchers have investigated a wide variety of fingertip sensors for robotic applications [1], [2], [3], [4]. These studies largely focus on capturing force data, a critical element for effective grasping and in-hand manipulation. Most sensors are designed to measure either localized point-contact forces or distributed forces over the contact area using mechanisms based on piezoelectricity, resistive, capacitive, or optical principles[5],[6].

Recent advancements in industrial force sensor technology have made it possible to miniaturize these devices so that they can be embedded directly in the fingertip[7]. For example, the DLR Hand2 integrates a six-axis force/torque sensor into its fingertip, providing precise force and torque feedback that enhances the development of sophisticated planning and control algorithms[8].

However, relying solely on force and torque measurements does not fully exploit the potential of tactile sensing. While force and torque provide essential feedback for motion control, accurate contact detection, localization, and the assessment of surface properties such as texture and geometry are equally crucial for effective object interaction[9].

Existing tactile sensing systems, such as the five-fingered Gifu3 hand, integrate force sensors with tactile sensors that track electrical current variations to detect contact events[10]. While these systems improve tactile perception, they still lack comprehensive techniques for analyzing surface texture characteristics and detecting unintended motion in real-time[11], limiting their ability to perform more complex tasks such as object reconstruction and precise motion planning[12].

Building on these gaps in previous research, this study presents a novel tactile sensing system that not only captures force and torque data but also enhances contact position localization, surface texture analysis, and unintended motion detection[13],[14]. The main focus of this research is the integration of a six-axis force/torque sensor with advanced algorithms that estimate an object's center of gravity (CoG) and utilize tactile feedback for object identification[15]. This work aims to bridge the gap between low-level tactile data and higher-level object understanding, enabling more sophisticated robotic manipulation and interaction[16].

1.1 Related Work

Over the past few decades, foundational research has explored tactile sensing that leverages force/torque measurements. Tsujimura et al. [17] introduced a method for pinpointing contact locations using an insensitive probe to capture object shape, which was later refined by Zhou et al. [18] by removing gravitational influences. Bicchi et al. [19] extended this work to estimate both the point of contact and its direction, further adapting their approach to accommodate soft-finger interactions. More recent studies have focused on discerning contact types through force/torque data. For instance, Murakami et al. [20] proposed a technique for determining the direction of a contact line, while Yamada et al.[21] employed a disc-shaped fingertip to extract both contact location and direction, introducing methods to distinguish among point, line, and planar contacts. Melchiorri et al. [22] tackled slip detection by developing a method that leverages force/torque signals to counteract both translational and rotational slips. Similarly, Jamali et al. [23] advanced texture sensing is achieved by integrating strain gauges and Polyvinylidene Fluoride (PVDF) films into a fingertip sensor, and later employed frequency-domain analysis to differentiate between textures[24],[25],[26].

1.2 Our Work

Fig. 1(a) shows the prototype of our fingertip sensor, featuring a hemispherical tip made from half of a table tennis ball, chosen for its clear geometry, which aids in precise contact detection. Beneath the fingertip is a 6-axis force-torque sensor (Sunrise Instrument M3701A); its industrial-grade construction ensures that high-precision force and torque data are reliably obtained.

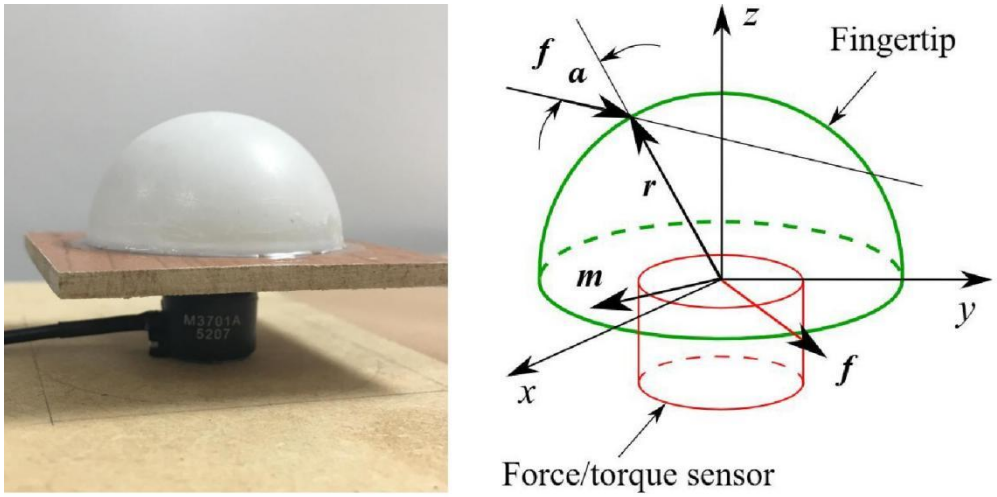

Figure 1. Prototype of the tactile fingertip sensor. (a) A 6-axis force-torque sensor mounted under a half table tennis ball. (b) Fingertip's mathematical model representing its geometric and mechanical properties.

Using these measurements, we have developed methods to determine the contact position and normal for point contacts. Additionally, by analyzing the force signals, the sensor can detect unintended motions like sliding, separation, and rolling. We further extract both frequency and amplitude features to perform texture analysis. The sensor has been integrated into a four-fingered hand, as shown in Fig.7(a), to expand its perceptual capabilities. With data from multiple fingers, we propose an algorithm to estimate an object' s center of gravity (CoG), complete with an analytical expression for error propagation in the estimation process. In addition, a neural network that utilizes both contact identification and CoG data is employed to classify basic objects—specifically spheres, cylinders, and cuboids. Finally, we present examples of object reconstruction to demonstrate the overall effectiveness of our approach.

2. Determining Contact Location and Orientation

Knowing the precise contact point and the corresponding surface normal is essential for ensuring grasp stability and for applying the correct contact forces during manipulation. Although many theoretical models assume that such data is readily available, practical sensors that can measure these quantities are rare. Our approach addresses this need by directly capturing the contact point and normal on the fingertip surface. With a hemispherical design, the contact normal is straightforwardly derived from the known geometry once the contact location is identified. Importantly, although our prototype uses a hemispherical fingertip for demonstration, this approach is applicable to any surface with known geometric properties.

As illustrated in Fig.1(b), our approach combines force and moment measurements with the known geometry of the fingertip to accurately determine the contact location and orientation - a concept originally introduced in [17]. Here, we summarize the key idea.

Assuming a point-contact model, the contact generates a pure force, and the sensor records the force vector f along with the moment m relative to the fingertip's world coordinate frame (see Fig.1(b)). When only a single contact is present, f directly represents the contact force, and the moment is given by:

$$m = -\hat{f}p \quad \text{[Formular 1]}$$

In this formulation, $p \in \mathbb{R}^3$ denotes the contact position relative to the fingertip frame, and $\hat{\mathbf{f}} \in \mathbb{R}^{3\times3}$ represents the skew-symmetric matrix corresponding to the cross product with f. Since $\hat{f}$ has rank two, the general solution for *p* can be written as:

$$p = -\hat{f}^{+}m + cd \quad \text{[Formular 2]}$$

Here, $\hat{f}^{+}$ denotes the pseudoinverse of $\hat{f}$, d is a basis vector spanning the null-space of $\hat{f}$, and c is a scalar constant. Eq.2 defines a line within the fingertip frame, which intersects the fingertip surface at two distinct points (as depicted in Fig.1(b). Using the known surface geometry, both intersection points and their associated normals can be calculated. The true contact point is identified as the one whose inward normal yields a positive dot product with f, consistent with the compressive nature of the applied force.

3. Identification of Unintended Motions

During grasping and in-hand manipulation, unintended movements such as sliding, separation, and rolling can occur, often leading to execution failures. Therefore, detecting these motions effectively is a crucial capability of a tactile sensing system[27],[28].

3.1 Sliding

Sliding happens when the fingertip moves relative to the object while still in contact. As established in Section2, the contact normal n can be determined. Additionally, the force vector f is directly obtained from the force/torque sensor. The angle between n and f can thus be computed. Based on Coulomb's friction law, if this angle exceeds the frictional threshold, sliding is taking place.

To simulate sliding, we applied vertical pressure on a plastic board using the fingertip and introduced horizontal forces in two different ways: first, by applying a sudden force and second, by gradually increasing the force until sliding initiated. The preliminary results, illustrated in Fig.2, indicate that abrupt increases in the inclination angle should be closely monitored as they signify the onset of sliding.

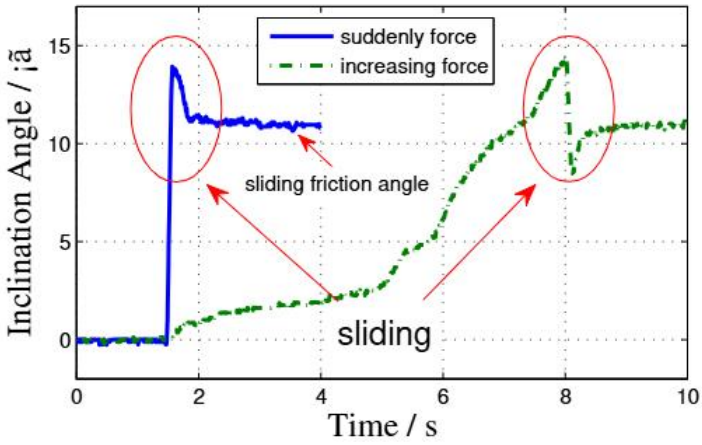

Figure 2. Simulation of sliding

3.2 Separation

Since real-time force and torque data are continuously available from the sensor, detecting object separation is straightforward. A significant drop in measured force or torque signals that the object is losing contact with the fingertips.

3.3 Rolling

If neither sliding nor separation is detected, but the contact point shifts across the fingertip surface, rolling is occurring. Unlike sliding, rolling maintains an inclination angle smaller than the frictional threshold, with only the contact location changing.

By accurately detecting these undesired motions, corrective actions such as motion adjustments, grip reinforcement, or regrasping strategies can be implemented to enhance grasp stability.

4. Feature Extraction for Texture Sensing

This section examines the potential of force/torque data in detecting surface textures. As classifiers based on reliable features are straightforward to implement, our main goal is to develop meaningful and robust feature representations.

From a microscopic perspective, texture arises from the surface's unevenness, where peaks and valleys create different stimuli upon contact. To characterize texture more effectively, we analyze two key aspects: pattern and roughness. If the surface irregularities are pronounced, the focus is on pattern recognition. Conversely, when the surface irregularities are subtle, roughness becomes the primary distinguishing factor. By leveraging both aspects, we can develop a more comprehensive texture classification system.

4.1 Pattern Recognition

In human skin, Meissner's corpuscles detect changes in surface contact, making frequency domain analysis a natural approach for pattern recognition [23].

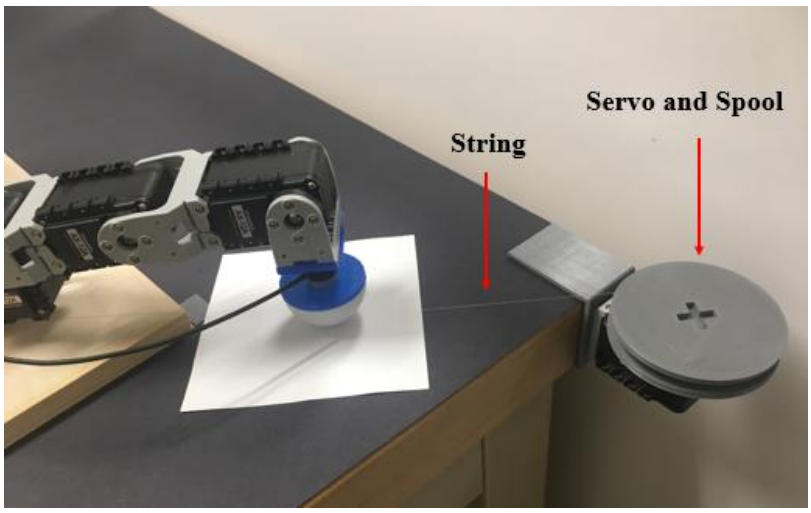

Figure 3.Experiment setup for texture sensing

As illustrated in Fig.3, the fingertip is pressed vertically onto the test material with a constant force of approximately 1N (equivalent to the gravitational force of the finger). A servo motor with a spool then pulls the material using a string at a steady velocity of 0.035m/s. The sampling rate is set to 200Hz. This setup enables us to collect force signals in the time domain, as shown in Fig.4 for a corrugated cardboard sample (Fig.5(a)). To simplify analysis, the string is aligned with the sensor's x-axis, ensuring that the measured tangential force corresponds to the x-component. This approach can be generalized using the known contact normal direction (Section2).

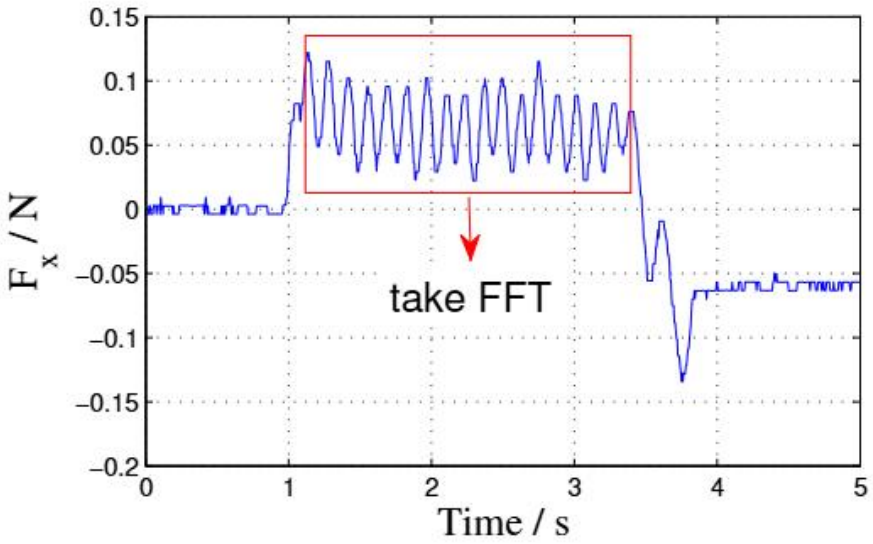

Figure 4. A time-domain example of Corrugated Cardboard 1

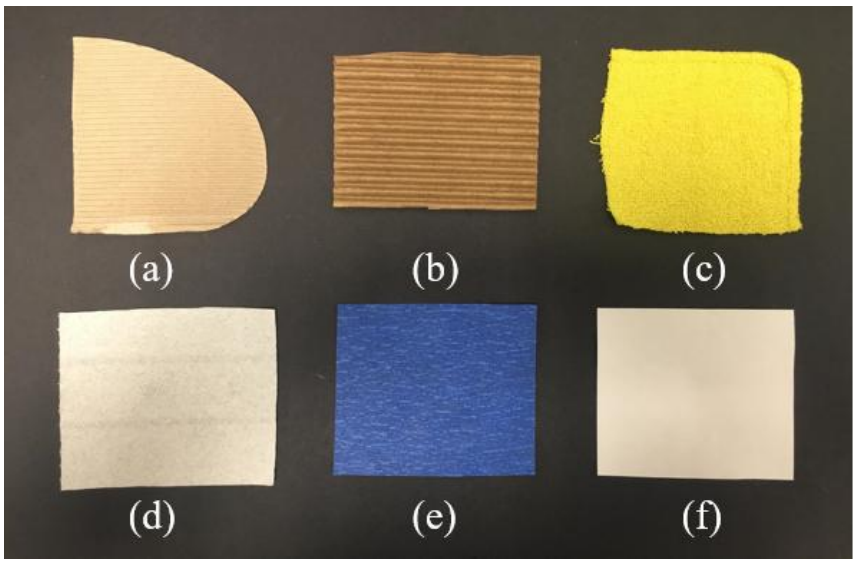

Figure 5. Materials. (a) Corrugated Cardboard 1 (b) Corrugated Cardboard 2 (c) Towel (d) Paper Towel (e) Painter's Tape (f) Copy Paper

Next, we apply the Fast Fourier Transform (FFT) to the force signals recorded during sliding (marked by the red square). Since sliding detection is already established (Section3), this transformation allows us to analyze the frequency characteristics of different textures.

For our experiments, we selected a variety of common materials, including two types of corrugated cardboard, a towel, paper towel, painter’ s tape, and copy paper, as shown in Fig. 5.

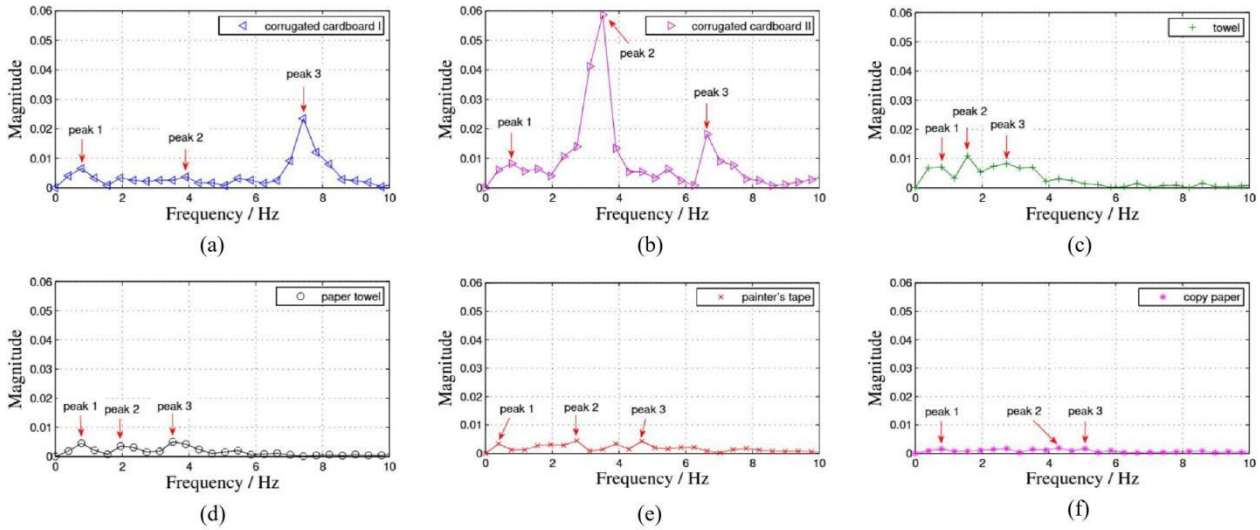

Figure 6.Frequency responses of different materials

The frequency analysis results, shown in Fig.6, focus on components below 10Hz due to the relatively slow pulling speed. As observed in prior studies[23], finer textures tend to generate higher-frequency signals than coarser surfaces. This trend is evident in our results, where the dominant frequency for corrugated cardboard1 (7.42Hz) is higher than that of corrugated cardboard2 (3.52Hz),

corresponding to their respective corrugation intervals of 5mm and 10mm.

The frequency peaks reflect the periodicity of the surface pattern, while their amplitudes indicate the prominence of the texture. To capture meaningful texture features, we select the most significant peaks, prioritizing those with higher amplitudes. Given that some materials exhibit non-uniform patterns and potential sensor noise, selecting multiple peaks is reasonable. As shown in Table1, we extract the three most prominent frequency peaks for pattern-based texture classification.

Table 1. Frequency Features for Texture Sensing

M.	Peak 1 (freq)(mag)		Peak 2 (freq)(mag)		Peak 3 (freq)(mag)	
(a)	0.8	6.5	3.9	3.7	7.4	23.5
(b)	0.8	8.3	3.5	58.6	6.6	18.2
(c)	0.8	7.1	1.6	10.9	2.7	8.3
(d)	0.8	4.5	2.0	3.5	3.5	5.0
(e)	0.4	3.4	2.7	4.5	4.7	4.4
(f)	0.8	1.6	4.3	1.9	5.1	1.7

Note: (a)--(f) are corresponding materials in Fig. 5.Units for frequency and magnitude are Hz and 10^{-3}, respectively.

4.2 Roughness Estimation

For surfaces with finer-scale irregularities (less than 1mm) or small protrusions, frequency analysis alone is insufficient, as the induced force variations may be too subtle relative to noise. In these cases, roughness is a more suitable characteristic for differentiation.

To quantify roughness, both amplitude and frequency components must be considered. While frequency-based features are extracted as described in Section4.1, amplitude-based features provide additional insight into surface roughness. Instead of relying on direct force amplitude—which varies with applied pressure—we utilize the inclination angle as a roughness indicator.

In Section 3, we introduced sliding detection based on inclination angle estimation. According to Coulomb's friction model, during continuous sliding, the inclination angle remains stable and corresponds to the friction angle. The sliding friction coefficient, represented by tan(friction angle), serves as a key roughness metric. A rougher surface typically results in a larger sliding friction angle.

To extract meaningful features, we compute the maximum, minimum, and average inclination angles during sliding, as summarized in Table2. These values provide a robust measure of surface roughness, helping to distinguish between different materials.

Table 2 . Amplitude Features for Texture Sensing

Material	Inclination angle during sliding		
	Maximum	Minimum	Average
(a)	11.78	7.12	8.88

(b)	30.21	4.98	17.20
(c)	14.43	10.29	12.93
(d)	12.69	10.53	11.64
(e)	10.21	7.68	8.79
(f)	8.40	6.04	6.86

Note: (a)--(f) are corresponding materials in Fig. 5. Unit is degree.

4.3 Feature Analysis and Classification

This section presented texture sensing features that incorporate both frequency and amplitude-based metrics. Materials with well-defined patterns, such as corrugated cardboard1 and corrugated cardboard2, exhibit distinct frequency signatures. In contrast, smooth surfaces like copy paper lack prominent frequency components but demonstrate lower roughness values. Materials such as towels, paper towels, and painter’ s tape fall between these extremes.

By integrating both feature sets, we can develop an effective classification model. Assigning appropriate weights—such as emphasizing high-amplitude frequency peaks—further enhances the accuracy of surface texture recognition.

5. Center of Gravity (CoG)

By considering the tactile inputs from all fingertips of the robot hand along with the measurements discussed earlier, we seek to extract further information, such as the object's Center of Gravity (CoG). CoG is a crucial parameter for hand motion control, as it directly affects object balance and grasp stability[29],[30].

5.1 Center of Gravity (CoG) Estimation

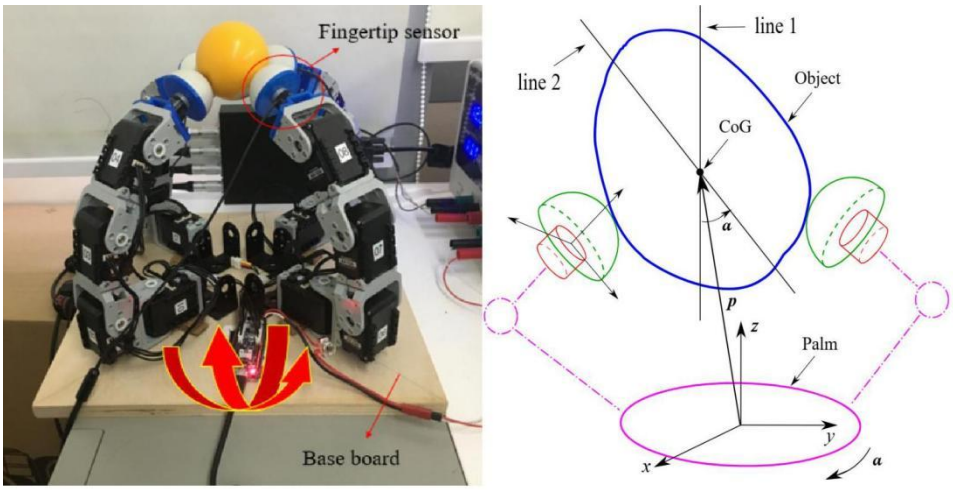

(a) (b)

Figure 7. Experimental setup. (a) A three-fingered hand outfitted with the proposed tactile fingertip sensors. (b) A mathematical model representing the experimental configuration.

Equipped with encoders that accurately measure joint angles, the robot hand provides the exact angle of each finger joint. Using forward kinematics, we calculate the position and rotation of each fingertip relative to the hand frame attached to the palm (see Fig. 7). Using this information, all forces and moments acting on the fingertips are transformed into a force F and a moment M in the hand frame. When the object is securely grasped and in static equilibrium, F represents the object's gravitational force, while M denotes the gravitational moment, expressed as

$$M = \hat{t}F = -\hat{F}t \cdots\cdots \text{[Formular 3]}$$

where t denotes the CoG position relative to the hand frame. The object's mass can be computed as $||F||/g$, where g represents gravitational acceleration. Solving Eq.3 for $t$yields

$$t = -\hat{F}^{+}M + cg = q + cg \cdots\cdots \text{[Formular 4]}$$

where g defines the basis of the null space of F, representing the gravitational direction in the hand frame.

Analogous to Eq.2, Eq.4 defines a straight line in the hand frame parallel to g. For instance, in the configuration shown in Fig.7(a), a downward-directed line (denoted as line1) is obtained, as illustrated in Fig.7(b). To refine the CoG estimation, we rotate the robot hand and the grasped object together while keeping the joint angles and contact positions constant. These parameters are monitored using the joint encoders and the sensing method described earlier. This rotation alters the gravitational direction g within the hand frame, yielding a new straight line, line~2, as illustrated in Fig.7(b). The intersection of these lines provides the estimated CoG position.

In practice, sensor inaccuracies may cause the computed lines in 3D space to not intersect precisely, resulting in skewed lines. To mitigate this, we collect multiple lines by rotating the robot hand into different orientations while keeping the object firmly grasped. The CoG is then determined as the point that minimizes the sum of squared distances to all these lines.

The squared perpendicular distance from a point to a line is given by

$$\begin{aligned} d(\mathbf{t}; q, \mathbf{g}) &= \| (q-t) - ((q-t)^T g)g \|^2 \\ &= \| (I - gg^T)(q-t) \|^2 \\ &= (q-t)^T (I - gg^T)(q-t) \end{aligned} \quad \cdots\cdots \text{[Formular 5]}$$

With N collected lines, the total squared distance is

$$D(t; q, g) = \sum_{i=1}^{N} (q_i - t)^T (I - g_i g_i^T)(q_i - t) \cdots \text{[Formular 6]}$$

where q_i and g_i correspond to values from Eq.4 for the i-th line.

To minimize this total squared distance, we take the derivative with respect to t:

$$\frac{\partial D}{\partial t} = \sum_{i=1}^{N} -2(I - g_i g_i^T)(q_i - l) = 0 \cdots\cdots \text{[Formular 7]}$$

Rearranging Eq.7, we derive

$$At = b \cdots\cdots \text{[Formular 8]}$$

Where $\mathrm{A} = \sum_{\mathrm{i}=1}^{\mathrm{N}} \left(\mathrm{I} - \mathrm{g_i g_i^T}\right)$ and $\mathrm{b} = \sum_{\mathrm{i}=1}^{\mathrm{N}} \left(\mathrm{I} - \mathrm{g_i g_i^T}\right) \mathrm{q_i}$.

Since g defines the null-space basis of $\mathrm{f_{ree}}$, we can select g as $\mathrm{f_{res}}$, simplifying b to $\sum_{i=1}^{N} q_i$. Consequently, the estimated CoG position $\hat{t}$ is given by

$$\hat{t} = A^{+}b \cdots\cdots [\text{Formular 9}]$$

5.2 Accuracy Test

In this section, we evaluate the precision of our CoG estimation method. As illustrated in Fig.7(a), our experimental hand comprises four fingers, each outfitted with a sensor prototype. Once the object is securely grasped, we begin by estimating the four contact positions and corresponding normals using the algorithm described in Section2. Concurrently, the approach detailed in Section5 is employed to compute a single set of data for CoG estimation. To acquire additional data, we alter the hand's pose while keeping the contact points unchanged. Since our hand lacks a wrist, we manually reorient the base board. Although at least two data sets are necessary to resolve the intersection for CoG estimation, we collect 10 sets in our experiments to enhance robustness, thereby compiling the full tactile dataset.

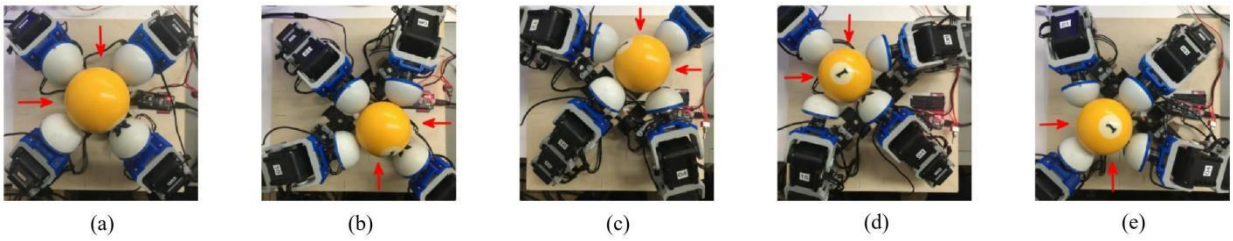

Figure 8. Accuracy test of different poses. (a) mid (b) bottom right (c) top right (d) top left (e) bottom left

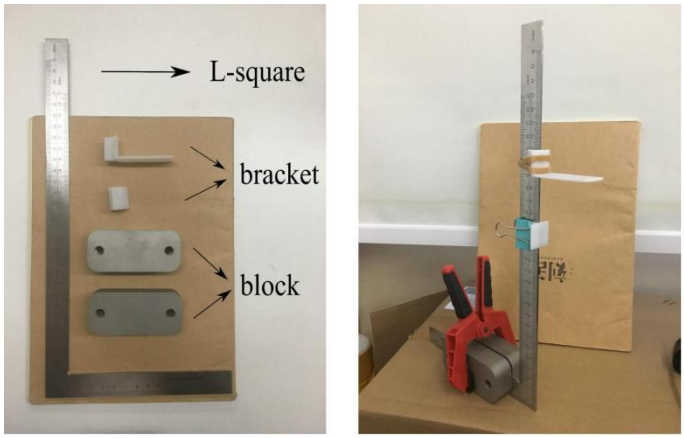

Figure 9. Testing tool.

For the accuracy test, a billiard ball was chosen as the test object due to its ideal spherical shape and uniform mass distribution. Measurements were acquired from five distinct top-view poses—namely, mid, bottom right, top right, top left, and bottom left—as shown in Fig.8. To establish the ground truth for the CoG, we employed a measurement tool consisting of an L-square, blocks, and brackets (see Fig.9). Given the known dimensions of the base board (300mm*300mm) and the billiard ball (d=57mm), the tool was moved along two perpendicular directions (as indicated by the red arrows in Fig.8), enabling CoG measurement with a precision of up to 0.5mm. Table3 compares the estimated

CoG values with the ground truth, showing that the typical error is below 5mm.

5.3 Experiment

CoG is a crucial parameter estimated through tactile feedback, offering insights beyond visual observation. In this experiment, we use our method to assess whether a nontransparent cup contains water and detect liquid motion.

Typically, when one wants to verify if a cup contains water, the common approach is to shake it. To emulate this, our experiment involves stirring the contents with a stick instead of shaking the cup. After removing the stick, we proceed with CoG estimation.

For an empty cup (i.e., a solid object), the CoG remains unchanged after agitation. As shown in Fig.10, the computed lines converge closely, indicating that the CoG is consistent.

However, if water is present, the CoG will vary as the liquid moves. At any given moment, only a single line can be determined to pass through the CoG, which implies that while we can detect a general shift in the CoG, pinpointing its exact position is approximate. Fig.11 illustrates two scenarios: one where the water is stirred laterally and another where it is stirred circumferentially. In both cases, the traced lines reflect the water's motion, corresponding to the dynamic change in CoG. Notably, these lines typically intersect at a single point due to centrifugal force. Water movement, modeled as a pendulum, generates a force detected by the outer fingers that converges at this point.

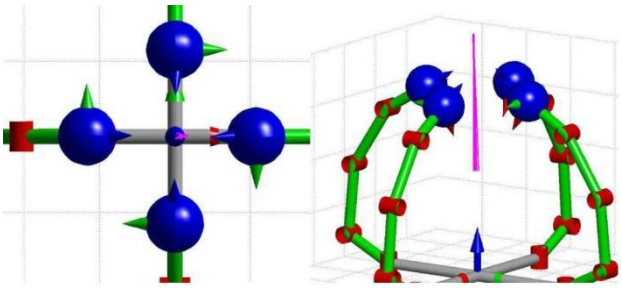

(a) (b)

Figure 10. CoG Estimation of a Solid Object. (a) Top view. (b) Side view.

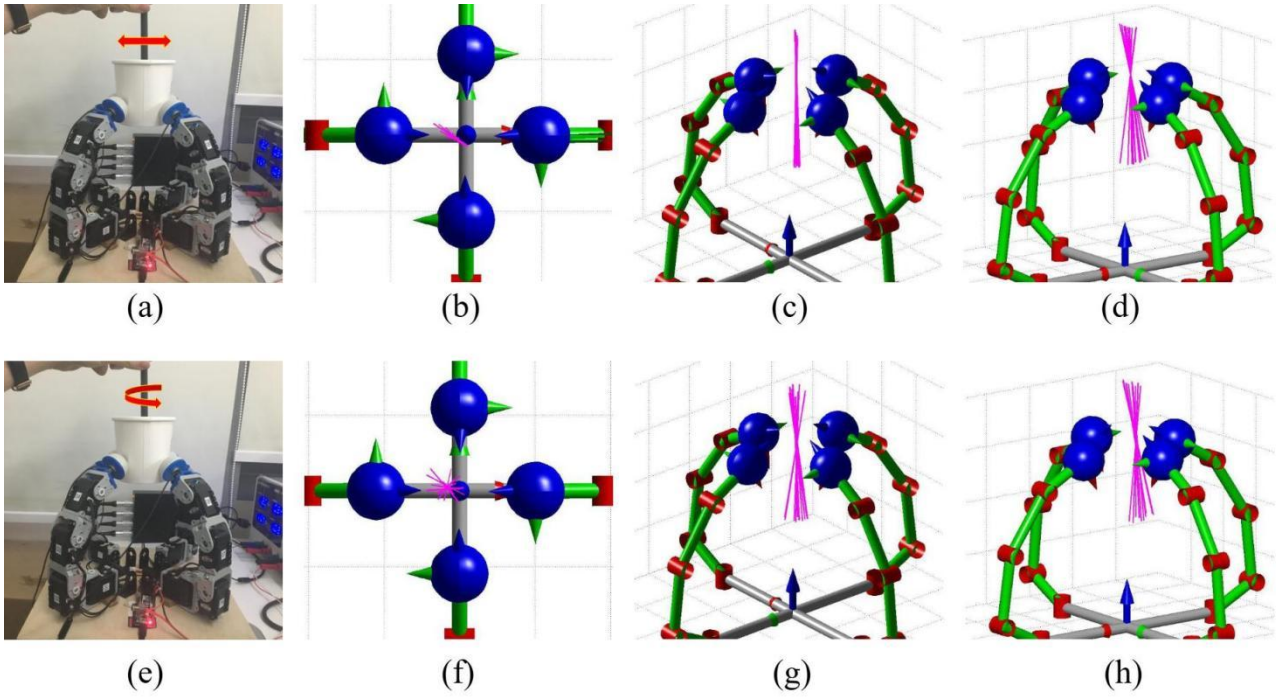

Figure 11. CoG Deviation Results. (a)--(d) Lateral Stirring. (e)--(h) Circumferential Stirring. (b)(f) Top view. (c)(g) Side view. (d)(h) Front view.

6. Object Classification and Reconstruction

Humans possess the remarkable ability to classify objects solely through local tactile feedback gathered during grasping and manipulation, without relying on vision. Inspired by this capability, we propose a method for object classification and reconstruction using a robotic hand equipped with tactile sensing.

Assuming the robotic hand grasps an object with m fingertips, our proposed techniques allow us to accurately determine the positions and surface normals at each of the m contact points. Using this geometric information, the robotic hand is capable of classifying basic object shapes, such as spheres, cylinders, and cuboids.

In this study, we focus on classification based on a single grasp. However, in future work, we aim to classify objects with more complex geometries by leveraging multiple grasps or employing in-hand manipulation techniques. Once classification is achieved, we further introduce strategies to reconstruct the object's shape based on the acquired contact information.

6.1 Classification

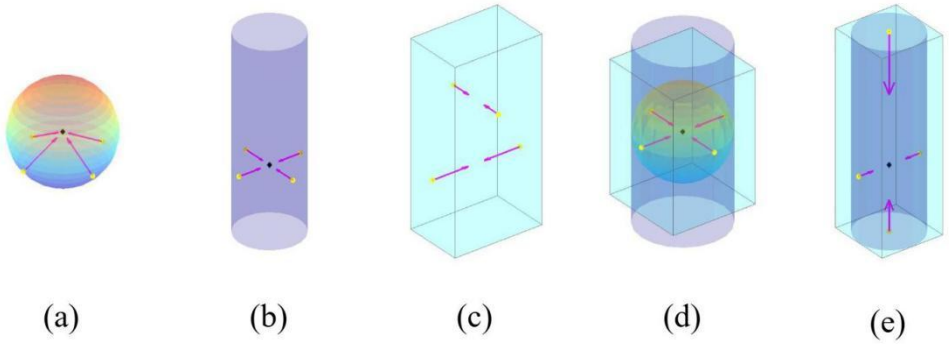

Figure 12. Theoretical illustrations. Yellow dots represent contact positions, pink vectors indicate contact normals, and the black diamond dot marks the intersection of contact normals. (a) A typical sphere. (b) A typical cylinder. (c) A typical cuboid. (d) Ambiguous case among a sphere, cylinder, and cuboid. (e) Ambiguous case between a cylinder and cuboid.

Table 3. CoG Estimation VS Ground Truth

Tests	Estimation(mm)			round Truth(mm)		
	$\hat{x}$	$\hat{y}$	$\hat{z}$	x	y	z
(a)	-4.4	-3.6	175	-2.1	-1.4	176
(b)	40.6	-2.7	136	42.1	0.4	136
(c)	-5.4	42.0	134	-0.7	41.0	136
(d)	-37.6	-1.6	138	-38.2	0.7	136
(e)	-0.8	-42.4	143	-0.7	-39.6	141

Note: (a)--(e) are corresponding locations in Fig. 8.

Distinct tactile patterns emerge for the three object types under consideration. For example, a sphere exhibits the characteristic that all contact normals converge at a single point (see Fig.12(a)), and the distances from this intersection point (i.e., the sphere's center) to each contact point are uniform, corresponding to the sphere’ s radius.

In the case of a cylinder, as illustrated in Fig.12(b), when grasping its curved surface, the contact normals are arranged perpendicular to the cylinder's central axis. These normals can be projected onto a common plane, where they intersect at a single point, reflecting the inherent geometry of the cylinder.

For a cuboid, the observed pattern is that the contact normals tend to be either orthogonal or directly opposite to one another (refer to Fig.12(c)).

Nevertheless, there are occasional ambiguous scenarios (Figs.12(d) and 12(e)) where classification based solely on one grasp may be unclear. In such cases, a simple regrasp or additional manipulation can resolve the ambiguity—an approach we plan to explore in future work.

To handle these ambiguous cases and to extend the classification to objects with irregular shapes, we propose a neural network-based approach that also accounts for hardware-induced errors.

For this purpose, we employ a two-layer feed-forward neural network. The hidden layer uses sigmoid activation functions, while the output layer employs softmax units, ensuring robust

classification of the input vectors. Trained with scaled conjugate gradient backpropagation, the network accepts 4 contact positions and 4 contact normals as input, yielding eight 3-Dimensional vectors (24 features in total). For our proof of concept, we configured the hidden layer with 50 neurons; further fine-tuning of the network architecture remains a future consideration.

The training dataset was partitioned into 70% for training, 20% for validation, and 10% for testing. As shown in Fig.15, we utilized six objects (two per object type) for training-collecting 15 samples for each object, amounting to 90 training samples-and three additional objects for testing, with 10 samples each (totaling 30 test samples). The results, depicted in Fig.13, demonstrate a classification accuracy approaching 100%.

Out of these, 3 samples were misclassified. Notably, their classification output probabilities for the assigned class were only slightly above 50%, indicating that these samples are near the decision boundary. To further illustrate this point, we have plotted these 3 configurations in Fig.14, which confirms our observation. This finding suggests that if the classification confidence falls below a certain threshold, the result should be considered unreliable. For instance, when applying a threshold of 90% confidence, an additional 4 samples are identified as being in ambiguous regions and would benefit from a regrasp or further manipulation to clarify the classification. Combining a 90% confidence criterion with a supplementary regrasp operation would yield a very high overall classification accuracy.

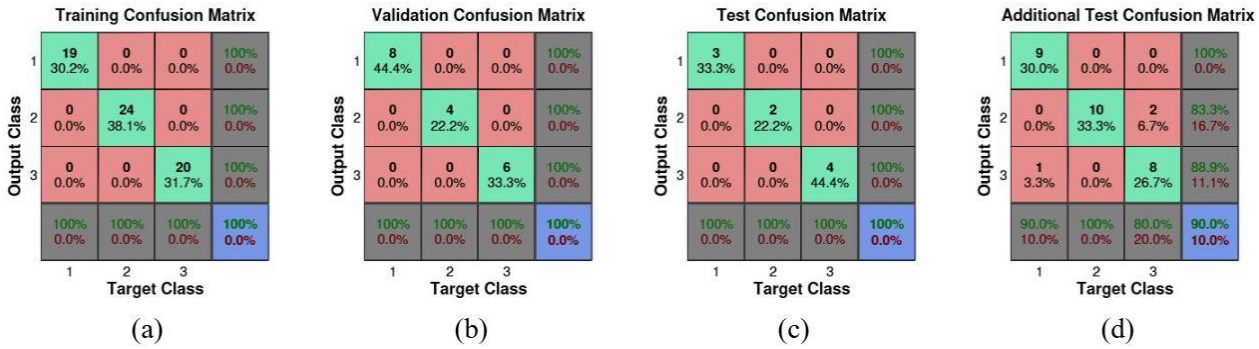

Figure 13. Confusion matrices. Classes 1, 2, and 3 represent sphere, cylinder, and cuboid, respectively. (a) Training confusion matrix. (b) Validation confusion matrix. (c) Testing confusion matrix. (d) Additional testing confusion matrix.

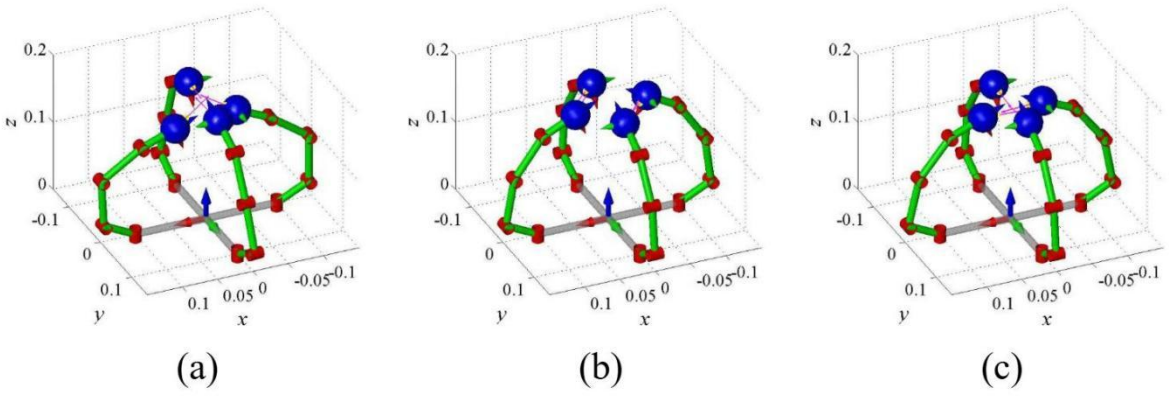

Figure 14. Misclassifications. (a) Sphere misclassified as cylinder. (b)(c) Cuboid misclassified as cylinder.

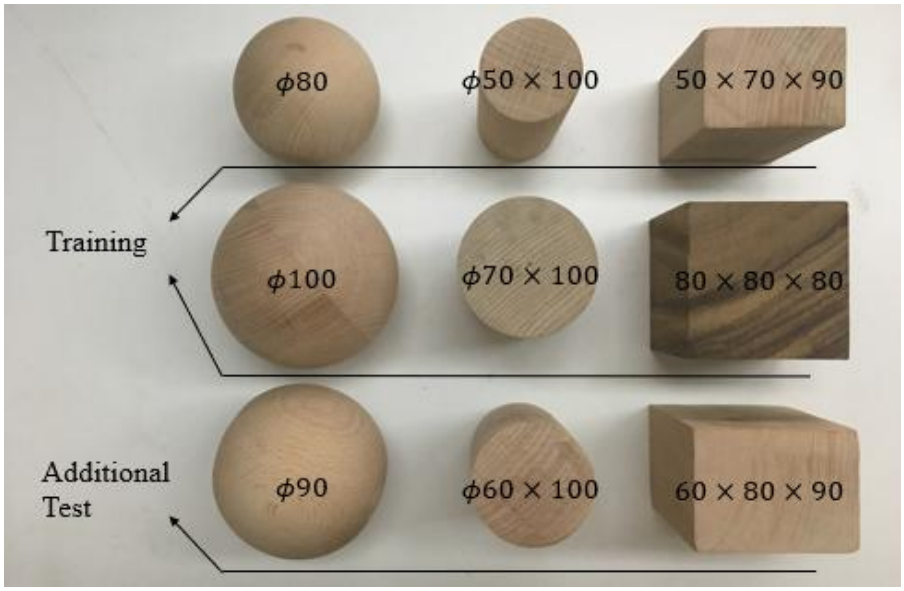

Figure 15. Objects (Unit: mm).

6.2 Reconstruction

Once the object has been classified, its geometric shape can be reconstructed using tactile feedback, including contact positions, contact normals, and the estimated CoG. We demonstrate our reconstruction strategy using three instances with classification confidences very close to 100%.

6.2.1 Sphere

For a sphere, we first estimate the radius by averaging the distances between the contact positions and the intersection point of the corresponding contact normals. This estimated radius, together with the intersection point, is then used to reconstruct the sphere as shown in Fig.16(d). The computed radius of 44.5mm closely matches the ground truth of 45mm.

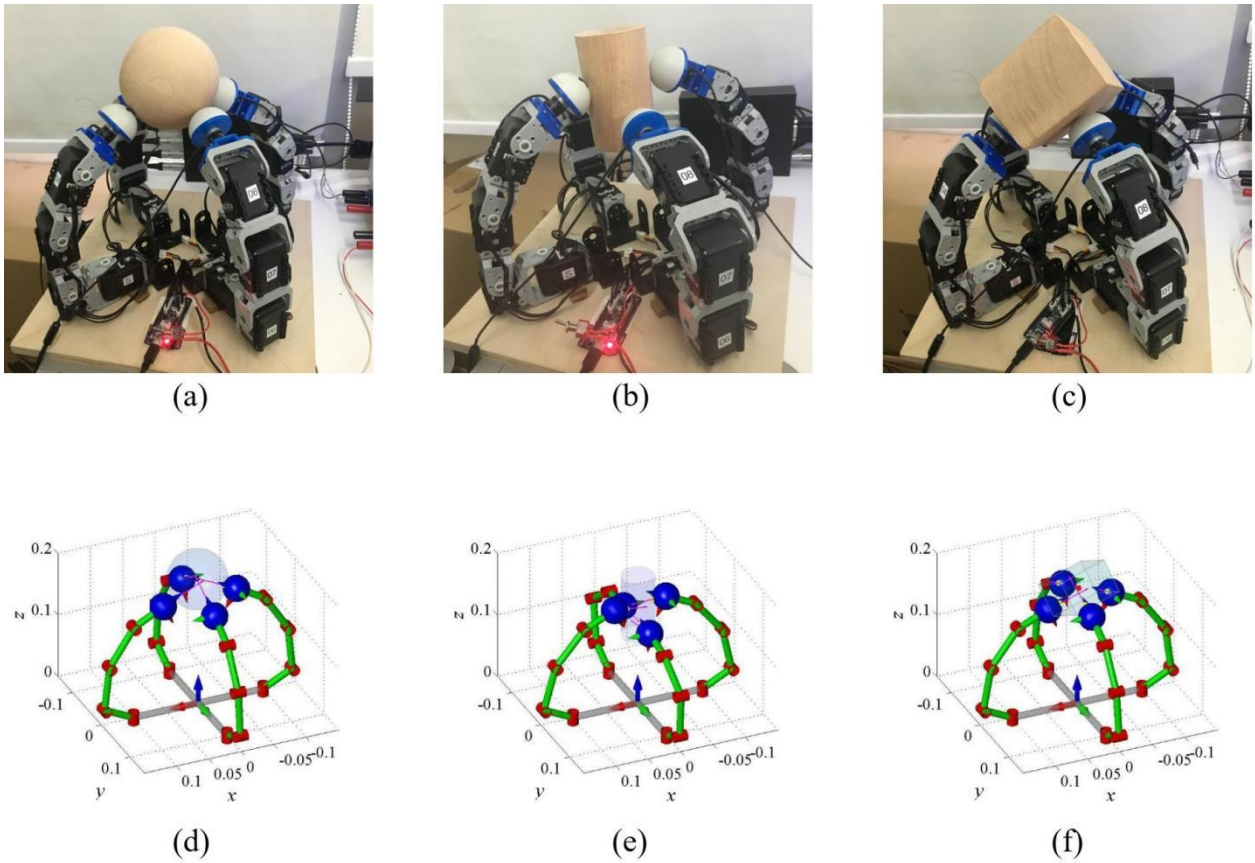

Figure 16. Results of Reconstruction. (a) Example of sphere. (b) Example of cylinder. (c) Example of cuboid.(d)(e)(f) Simulation Results. The yellow dots indicate contact positions, the pink vectors represent contact normals, the red dot marks the estimated CoG, and the black diamond dot denotes the intersection of contact normals.

6.2.2 Cylinder

In the case of a cylinder, the robot hand grasps the object on its curved surface, which allows us to reconstruct only the cylindrical portion (see Fig.16(e)). The procedure begins by determining the vector that is most perpendicular to the set of contact normals. This vector defines a common plane onto which the contact normals are projected. Within this plane, the projected normals converge at a single point. The average distance from this intersection point to the projected contact positions is then computed to estimate the radius. Using this radius along with the intersection point, the cylindrical surface is reconstructed, yielding an estimated radius of 25mm (with the ground truth being 30mm).

6.2.3 Cuboid

For a cuboid, as depicted in Fig.16(f), the reconstruction process is slightly more complex. In this scenario, two of the contact normals are parallel, indicating they represent the same face dimension. The remaining two normals, together with these, are oriented orthogonally, thereby capturing the three distinct dimensions of the cuboid. Assuming the object is homogeneous, its CoG

coincides with its geometric center. With the estimated CoG and the local contact positions and normals, the contact surfaces can be reconstructed. By computing the distances from the CoG to these surfaces, the dimensions of the cuboid are determined. In our experiment, the estimated dimensions were 50mm*73mm*88mm compared to the ground truth dimensions of 60mm*80mm*90mm.

7. Summary and Future Work

In this work, we presented a novel tactile fingertip sensor capable of concurrently measuring contact positions and normals, as well as detecting unintended motions such as sliding, separation, and rolling. We also introduced frequency and amplitude-based features for texture sensing and proposed a multi-finger approach to estimate the object's center of gravity (CoG), including an analysis of error propagation. An artificial neural network was utilized to classify objects—spheres, cylinders, and cuboids—and we demonstrated three reconstruction examples with a four-fingered robotic hand. The preliminary results are promising, demonstrating the effectiveness of the proposed system in enhancing robotic tactile perception.

The primary focus of this research is to integrate multi-dimensional tactile feedback for improved object interaction and identification. By combining force/torque data with detailed tactile sensing, our work advances the capability of robotic hands to perform sophisticated tasks such as object reconstruction and precise manipulation.

Looking forward, several future directions have been identified. First, we plan to explore in-hand manipulation strategies to facilitate regrasping, addressing situations where a single grasp may be insufficient due to ambiguity. Second, we aim to enhance our algorithms to better address undesired motions and surface classification, as well as implement active touch motions for improved texture sensing. Third, by leveraging in-hand manipulation, we anticipate collecting richer local tactile data, which would be beneficial for identifying more complex objects. Additionally, we are investigating hardware improvements, such as incorporating a wrist joint to reduce the need for human intervention and improve the system's overall performance. Ultimately, our goal is to develop a tactile sensing system that can match human proficiency, significantly advancing the field of robotic perception.

References

[1] Dahiya, R.S., Metta, G., Valle, M. and Sandini, G. Tactile sensing—from humans to humanoids. IEEE Transactions on Robotics, 2009, 26(1), 1–20.

[2] Cutkosky, M.R. and Provancher, W. Force and tactile sensing. In: Springer Handbook of Robotics, 2016, 717–736.

[3] Yousef, H., Boukallel, M. and Althoefer, K. Tactile sensing for dexterous in-hand manipulation in robotics—A review. Sensors and Actuators A: Physical, 2011, 167(2), 171–187.

[4] Saudabayev, A. and Varol, H.A. Sensors for robotic hands: A survey of state of the art. IEEE Access, 2015, 3, 1765–1782.

[5] Zhang, L., Liu, J., Wei, Y., An, D. and Ning, X. Self-supervised learning-based multi-source spectral fusion for fruit quality evaluation: A case study in mango fruit ripeness prediction. Information Fusion, 2025, 117, 102814.

[6] Huang, J., Yu, X., An, D., Ning, X., Liu, J. and Tiwari, P. Uniformity and deformation: A benchmark for multi-fish

real-time tracking in the farming. Expert Systems with Applications, 2025, 264, 125653.

[7] Zhang, H., Yu, L., Wang, G., Liu, Y., Yang, Y. and Zhang, G. Cross-modal knowledge transfer for 3D point clouds via graph offset prediction. Pattern Recognition, 2025, 162, 111351.

[8] Sun, H., Park, S. and Hwang, D. Compact modular robotic wrist with variable stiffness capability. IEEE Transactions on Robotics, 2024.

[9] Yang, J.-H., Kim, S.-Y. and Lim, S.-C. Effects of sensing tactile arrays, shear force, and proprioception of robot on texture recognition. Sensors, 2023, 23(6), 3201.

[10] Wang, M., Li, W., Liang, H., Zhao, Y., Yang, H. and Zhu, Q. Large-scale deployment of vision-based tactile sensors on multi-fingered grippers. IEEE, 2024, 13946–13952.

[11] Masoumi, N., Ramos, A.C., Torkaman, T., Li, Q., Bayat, M. and Nahavandi, S. Embedded force sensor for soft robots with deep transformation calibration. IEEE Transactions on Medical Robotics and Bionics, 2024.

[12] Liu, X., Zhang, B., Wang, L., Chen, X., Huang, Y. and Wu, Y. Fine-grained recognition of manipulation activities on objects via multi-modal sensing. IEEE Transactions on Mobile Computing, 2024, 23(10), 9614–9628..

[13] Yu, L., Zhang, X., Zhong, Z., Lai, Y., Zhang, H. and Szczerbicki, E. Adaptive2Former: Enhancing chromosome instance segmentation with adaptive query decoder. Cybernetics and Systems, 2023, 1–9.

[14] Pokhrel, K., Sanin, C., Sakib, M.K.H., Islam, M.R. and Szczerbicki, E. Improved skin disease classification with mask R-CNN and augmented dataset. Cybernetics and Systems, 2023, 1–15.

[15] Li, S. and Xu, J. Multi-axis force/torque sensor technologies: Design principles and robotic force control applications: A review. IEEE Sensors Journal, 2024.

[16] Pohtongkam, S. and Srinonchat, J. Object recognition for humanoid robots using full hand tactile sensor. IEEE Access, 2023, 11, 20284–20297.

[17] Tsujimura, T. and Yabuta, T. Object detection by tactile sensing method employing force/torque information. IEEE Transactions on Robotics and Automation, 1989, 5(4), 444–450.

[18] Zhou, X., Shi, Q. and Li, Z. Contact localization using force/torque measurements. IEEE, 1996, 1339–1344.

[19] Bicchi, A. Intrinsic contact sensing for soft fingers. IEEE, 1990, 968–973.

[20] Murakami, K. and Hasegawa, T. Tactile sensing of edge direction of an object with a soft fingertip contact. IEEE, 2005, 2571–2577.

[21] Yamada, T., Nakanishi, S., Yamamoto, H. and Johansson, R. Identification of contact conditions between fingers and a grasped object by active force sensing. IEEE, 2014, 1224–1229.

[22] Melchiorri, C. Slip detection and control using tactile and force sensors. IEEE/ASME Transactions on Mechatronics, 2000, 5(3), 235–243.

[23] Jamali, N. and Sammut, C. Material classification by tactile sensing using surface textures. IEEE, 2010, 2336–2341.

[24] Masenya, T.M. Digital transformation of medical libraries: Positioning and pioneering electronic health record systems in South Africa. International Journal of E-Health and Medical Communications (IJEHMC), 2024, 15(1), 1–13.

[25] Li, M. and Guenier, A.W. ChatGPT and health communication: A systematic literature review. International Journal of E-Health and Medical Communications (IJEHMC), 2024, 15(1), 1–26.

[26] Dong, L.Z. and Zhang, K. Does digital financial innovation contribute to promoting the high-quality development of the real economy? Mechanism analysis and spatial econometrics based on financial service efficiency. Journal of Xi'an University of Finance and Economics, 2024, 37, 60–72. DOI: 10.19331/j.cnki.jxufe.20231115.001

[27] Wang, Q., Ulloa, P.M., Burke, R., Bulens, D.C. and Redmond, S.J. Robust learning-based incipient slip detection using the papillarray optical tactile sensor for improved robotic gripping. IEEE Robotics and Automation Letters, 2023, 9(2), 1827–1834.

[28] Gao, J., Huang, Z., Tang, Z., Song, H. and Liang, W. Visuo-tactile-based slip detection using a multi-scale temporal convolution network. arXiv preprint arXiv:230213564, 2023.

[29] Puang, E.Y., Li, Z., Chew, C.M., Luo, S. and Wu, Y. Learning stable robot grasping with transformer-based tactile control policies. arXiv preprint arXiv:240721172, 2024.

[30] Kim, S., Jha, D.K., Romeres, D., Patre, P. and Rodriguez, A. Simultaneous tactile estimation and control of extrinsic contact. IEEE, 2023, 12563–12569.